Chemical Geology 697 (2025) 123125

Contents lists available at ScienceDirect

Chemical Geology

journal homepage: www.elsevier.com/locate/chemgeo

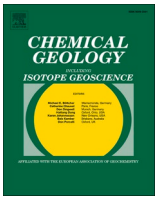

Unveiling rodingite metasomatism using B and Sr isotopes: Insights from the Voltri Massif, Western Ligurian Alps, Italy

E. Cannaò *

Dipartimento di Scienze della Terra "A. Desio", Università degli Studi di Milano, Via Botticelli 23, 20133 Milano, Italy

A B S T R A C T

The recycling of volatiles and incompatible elements at subduction zones is a key driver of Earth's geochemical evolution, with metasomatic reactions governing elemental fluxes. Rodingites, found at mafic–ultramafic interfaces, may transform into metarodingites during subduction, often accompanied by chlorite-rich blackwall zones. While these rocks are potential geochemical reservoirs, their role in boron (B) cycling remains unclear. This study presents new *in-situ* $\delta^{11}B$ data from chlorite, along with trace element and Sr isotope analyses of clinopyroxene and clinozoisite, from metarodingite–blackwall assemblages in the Voltri Massif (Western Ligurian Alps, Italy). The metarodingites exhibit assemblages of clinopyroxene + garnet + chlorite ± epidote, consistent with rodingitization under oceanic conditions. Preserved mantle-like $^{87}Sr/^{86}Sr$ and REE signatures in igneous clinopyroxene cores suggest limited overprinting by seawater-derived fluids. Trace element redistribution in metamorphic minerals (*e.g.,* HFSE loss, Eu anomalies) points to prograde subduction overprint, and Sr isotopes suggest seawater-derived recycling during burial. Chlorite $\delta^{11}B$ values vary spatially in metarodingites, reflecting differences in water/rock ratios and interaction with B-rich fluids during oceanic metasomatism. In contrast, blackwall chlorite shows more uniform $\delta^{11}B$, possibly due to Mg-metasomatism at high water/rock ratios and equilibration at the mafic–ultramafic boundary. Whether these signatures are oceanic or subduction-related remains unresolved, pending geochronological constraints. These data suggest chlorite may serve as a previously unrecognized B reservoir, releasing ^{11}B-enriched fluids during high-pressure breakdown, thereby influencing deep volatile cycling.

1. Introduction

Recycling of volatiles and incompatible elements at convergent margins reflects the dynamism of our planet (Bekaert et al., 2021), a feature distinguishing Earth from other terrestrial bodies. Prograde reactions within subducting slab act as geochemical filters, determining which elements can be returned to the surface through arc volcanism and which are retained in high and ultrahigh pressure (high-*P* and *UHP*) minerals, influencing the geochemical refertilization of the Earth's interior (*e.g.*, Cannaò and Malaspina, 2018). How these reactions work strongly depend on the lithologies involved in subduction processes, which encompass from ultramafic-mafic sequences to (meta)sedimentary and crustal rocks. The geochemical modification of these reservoirs can occur either through metasomatic processes during their exposure on the seafloor (*e.g.*, Bach et al., 2013), or by fluid-mediated chemical exchanges in subduction settings (*e.g.*, Bebout, 2013).

At oceanic stage, metasomatism can produce Ca-rich and Si- and Na-poor mafic rocks made of Ca-rich garnet + clinopyroxene + chlorite ± epidote ± vesuvianite, the so-called rodingites (*e.g.*, Frost, 1974; Rice, 1983). These rocks form during serpentinization of ultramafic rocks enclosing gabbro/basaltic dikes and are commonly characterized by variable fluid/rock ratios (Bach and Klein, 2009). Chlorite-rich blackwall surrounding rodingites may form along the lithological boundaries between ultramafic and mafic rocks either during an oceanic stage or prograde subduction evolution (Codillo et al., 2022; Frost, 1974; Laborda-López et al., 2018; Panseri et al., 2008; Shen et al., 2016; Spandler et al., 2008; Xiong et al., 2024; Zhao et al., 2023), reflecting a combination of infiltration and diffusion metasomatism involving fluid flow and mass transfer. At a bigger scale, metasomatic chlorite-schists can form along the subduction plate-interface generating mélange domains (Bebout and Barton, 2002), having important implications for plate-tectonic processes (Marschall and Schumacher, 2012).

Metamorphosed rodingites (*i.e.*, metarodingites) and associated chlorite blackwall represent hybrid geochemical reservoirs whose role in subduction element recycling remain poorly constrained (Cannaò et al., 2023b; Laborda-López et al., 2020; Spandler et al., 2008; Xiong et al., 2024). This is especially relevant for boron (B), a key tracer of surface-mantle interactions due to its high concentration in surficial reservoirs, low mantle concentration (Marschall et al., 2017), and high solubility in aqueous fluids (Moran et al., 1992). Boron, with two stable isotopes (^{11}B and ^{10}B), shows large isotope fractionation (Kowalski and Wunder, 2018), providing a unique tool to investigate geological

* Corresponding author.
E-mail address: enrico.cannao@unimi.it.

https://doi.org/10.1016/j.chemgeo.2025.123125
Received 25 June 2025; Received in revised form 14 October 2025; Accepted 31 October 2025
Available online 2 November 2025

processes. Besides tourmalines, serpentines and micas are the two main mineral repositories for B in subduction zones with concentrations spanning from tens to hundreds of μg/g. Oceanic serpentinites are commonly characterized by positive B isotope composition ($\delta^{11}B$) reflecting the interaction with seawater-derived fluids ($\delta^{11}B_{seawater} \sim +39.5$ ‰; Spivack and Edmond, 1987), whereas serpentinites from wedge-derivation generally display progressively negative $\delta^{11}B$ values, as the result of interaction with shallow *vs.* deep slab-derived metamorphic fluids (Martin et al., 2016). Negative $\delta^{11}B$ imprints in serpentinites have been recently documented also in oceanic ophicarbonates and related to variable composition of the hydrothermal fluid system (Cannaò, 2025; Cannaò et al., 2024). Micas generally have negative $\delta^{11}B$ (Ishikawa and Nakamura, 1993; Xu et al., 2022), although their high reactivity during metamorphic reactions in the presence of fluids may easily change their signatures towards higher values (Halama et al., 2020). Overall, prograde subduction reactions decrease the B inventory of the mafic and sedimentary rocks and decrease their $\delta^{11}B$ signatures due to high B mobility in fluids and the preferential fractionation of the heavy B isotope in the fluid phase (Konrad-Schmolke and Halama, 2014).

The role of chlorite as a B repository in subduction zones is poorly investigated (Marschall et al., 2006), and it is unclear how B isotopes are affected by chloritization (De Hoog and Savov, 2018). Chlorite is stable at higher P and T than serpentine (Pawley, 2003; Ulmer and Trommsdorff, 1995), and further investigations are required to understand its role as geochemical carrier of incompatible elements to greater depths. Recent studies proposed that *UHP* subduction of chlorite-rich metasomatic rocks along cold geotherms may stabilize hydrous Al-rich silicates, such as the 11.5 Å and Mg-sursassite (Hermann and Lakey, 2021), belonging to the so-called Dense Hydrous Magnesium silicates – DHMSs (Irifune et al., 1998). These phases may carry significant H_2O to the deep mantle (Iwamori, 2004), influencing the deep-water cycle over geological timescales, though their geochemical role remains poorly known (Cannaò et al., 2023a).

This contribution presents new geochemical data on chlorite from an association of metarodingite and blackwall, developed along the contact between metarodingite and high-*P* serpentinites from the Voltri Massif (Ligurian W. Alps, Italy). The *in-situ* $\delta^{11}B$ data on chlorite, along with the trace element inventories of rock-forming minerals and *in-situ* Sr isotope composition of clinopyroxene and clinozoisite, are used to better constrain the chemical evolution of these metasomatized lithologies. The documented $\delta^{11}B$ signature suggests that chlorite blackwall may represent an unaccounted reservoir able of transferring ^{11}B-rich fluids during dehydration at sub-arc conditions. Major implications for deep B recycle are also discussed.

2. Geological background and sample description

The Voltri Massif (Ligurian W. Alps) is an ophiolitic complex made of metamorphosed serpentinites and serpentinized mantle rocks associated with metasedimentary rocks (mica-, calc-schists and marbles) intercalated with metavolcanics of oceanic origin (Capponi et al., 2016). Mafic bodies of metamorphosed gabbroic and basaltic dikes are often enclosed within ultramafic rocks and metasediments (Cannaò et al., 2023b; Malatesta et al., 2012). Rodingites dikes occur embedded within serpentinites as witness of oceanic alteration on the seafloor (Cannaò et al., 2023b; Haws et al., 2021; Scambelluri and Rampone, 1999). According to structural-petrographic and geochemical-geochronological investigations, the Voltri Massif records initial oceanic alteration at ~160 Ma, followed by eclogite-facies subduction (1.8–2.5 GPa, 450–600 °C) in a timespan from 50 to 37 Ma, and exhumation at 35–25 Ma during the Alpine orogeny (Federico et al., 2007; Haws et al., 2021; Rubatto and Scambelluri, 2003; Scambelluri et al., 1995; Starr et al., 2020).

The area of study is located close to the top of the Bric Camulà, northwest of the village of Cogoleto (Genova, Italy), at approximately 820–750 m above the sea level (Supplementary Fig. S1). Variably deformed serpentinite is the dominant lithology in the area hosting several bodies of metamorphosed rodingites (Fig. 1). The metarodingitic bodies are smaller in size, from less than one meter to a few meters, and are displaced along the main serpentinite foliation. The serpentinite foliation is cut by olivine-bearing veins and shear bands, which testify the partial antigorite dehydration during prograde subduction at high-*P* (Fig. 1b). These field relations, similar to other occurrence within the Voltri Massif (Cannaò et al., 2016; Scambelluri et al., 1995; Scambelluri and Rampone, 1999), indicate that (meta)rodingite bodies were associated with serpentinites prior to the high-*P* stage.

Metarodingites mainly show a massive texture with garnet + clinopyroxene + chlorite as the main mineral assemblage (Fig. 1c, d, e, f), giving a pinkish-green colour on hand specimens. In some area, chlorite-rich metasomatic layers – *i.e.,* blackwall – are observed along the contact between the ultramafic and mafic lithologies (Fig. 1f) as well as within the rodingitic dikes along major fractures (Fig. 1e). The blackwall is dominated by chlorite with minor amount of coarse clinopyroxene and oxides as accessory minerals. Five samples of metarodingites with variable developed chlorite blackwall were collected, together with three samples of the host serpentinites (Table 1, Supplementary Figs. 1, 2).

The serpentinites still preserve relicts of the mantle pyroxene sites showing bastite texture made of serpentine + magnetite (Fig. 2a). The bastite are surrounded by serpentine + magnetite in mesh texture, indicating former olivine grains. Both mesh and bastite textures are locally overgrown by a new generation of foliated serpentine forming a shear bands texture (Fig. 2a), indicating complex evolution from oceanic to subduction stages. The metarodingites show preserved coarse grains of the protolith igneous clinopyroxene (turbid), only partially recrystallized along the rims (colourless and limpid; Fig. 2b, d). A second generation of clinopyroxene (colourless and limpid, cpx2) often occur in the matrix of the metarodingite together with the garnet (Fig. 2c, e, f, g) and its genesis can be related to either an oceanic hydrothermal event or to subduction evolution. At least two generations of garnet are recognized, the first one form a heavy ground mass and is darker in colour compared to the second generation of garnet, which is more limpid and colourless (Fig. 2b). The second generation of garnet is smaller in size and mostly displaced along grain boundaries or in small veins. Clinozoisite occurs only in the matrix of the samples BCR21–2A/B (Fig. 2c), where limited amount of chlorite is formed. Chlorite shows massive to foliated texture with evidence of recrystallization in both the host metarodingite and in the blackwall (Fig. 2c, g, h). Within the blackwall, static chlorite recrystallization is almost complete in sample BCR21–1B (Fig. 2h), while foliated chlorite is shown in sample BCE23 (Fig. 2g), which is coherent with the foliation of the host serpentinites (Fig. 1d).

3. Analytical methods

Mineral major element composition was determined using a JEOL Superprobe JXA-8200 hosted at the Earth Science Department "A. Desio", University of Milano LA STATALE (Italy). The analyses were conducted with a WDS system operating at 5 nA and 15.0 kV, and 1 μm beam size. Different international reference materials were used as standards: Mg on forsterite, Fe on fayalite, Na on omphacite, Ti on ilmenite, Mn on rodonite, K on k-feldspar, Al, Si and Ca on anorthite, and Cr on metallit/pure Cr, Ni on niccolite, and Cl on scapolite.

Identification of the serpentine polysome was carried out using an XploRA PLUS Horiba micro-Raman hosted at the Dipartimento di Scienze della Terra, Ambiente e Vita, University of Genova (Italy). The instrument was equipped with 532 nm laser with nominal power of 100 mW (set to 50 %) focused on the sample by an Olympus microscope with a 50× objective. The micro-Raman spectra were collected in the wavelengths corresponding to the vibration regions of the alumino-silicate network (200–1100 cm^{-1}) and of the O—H bond stretching (3600–3800 cm^{-1}). Each spectrum results from three acquisitions of 20 s each using grating of 2400 g/mm and analyzed by a CCD detector. A silicon wafer was used to check the calibration of the spectrometer at

Fig. 1. Field occurrence of serpentinites and metarodingites in the studied area. (A) Detail of a tectonite serpentinite showing main coarse trace of foliation (in yellow; sample BCS23–1). (B) Complex veins of metamorphic olivine crosscutting the main texture of the serpentinites (sample BCS23–3). (C) Body of metarodingite enclosed in serpentinite showing well-developed chlorite blackwall (sample BCR23). (D) Boudinated body of metarodingite (samples BCE21–1 and BCE23). (E) Strongly chloritized body of metarodingite enclosed in serpentinites (sample BCR21–1). (F) Detail of the sample BCR21–1 showing massive texture and a sharp

contact between metarodingite and chlorite blackwall. White grains of clinopyroxene (cpx) are visible within the garnet matrix (grt). (For interpretation of the references to colour in this figure legend, the reader is referred to the web version of this article.)

Table 1
Sample list and their main features.

Sample name	Section	Rock type	Texture	Main mineralogical assemblage	Coordinate (WGS84)	
					N	E
BCR21–1	A	Rodingite	Massive	chl1–2 + grt + cpx1–2	44° 25′ 12.1”	8° 37′ 18.3”
	B	Rodingite/Blackwall	Massive	chl1–2 + cpx1–2 ± ox		
BCR23	A	Rodingite	Massive	chl1–2 + grt + cpx1–2	44° 25′ 13.2”	8° 37′ 16.6”
	B	Blackwall	Foliated	chl1–2 + cpx1–2 ± ox		
BCR21–2	A	Rodingite	Massive (coarse texture)	cpx1–2 ± zo ± grt ± ox	44° 25′ 14.7”	8° 37′ 15.0”
	B	Rodingite	Massive (fine texture)	cpx1–2 ± zo ± grt ± ox		
BCE21–-1	A	Rodingite	Massive	grt + cpx1–2 + chl + ox	44° 25′ 14.5”	8° 37′ 15.7”
	B	Rodingite	Massive	grt + cpx1–2 + chl + ox		
BCE23		Rodingite/Blackwall	Foliated	chl1–2 + cpx1–2 ± ox	44° 25′ 14.5”	8° 37′ 15.7”
BCS23–1		Serpentinite	Tectonite	atg ± ox	44° 25′ 12.7”	8° 37′ 17.3”
BCS23–2		Serpentinite	Foliated	atg ± ox	44° 25′ 13.7”	8° 37′ 18.7”
BCS23–3		Serpentinite	Tectonite	atg ± ox	44° 35′ 05.5”	8° 27′ 20.4”

See Supplementary Fig. S2 for detail images of samples.

520.50 cm^{-1}.

In-situ trace element mineral composition was determined by laser ablation inductively coupled plasma mass spectrometry (LA-ICP-MS) hosted at the Geochemistry, Geochronology and Isotope Geology Laboratory of the Earth Science Department “A. Desio”, University of Milano LA STATALE (Italy). The instrumentation couples a 193 nm ArF excimer laser microprobe system (Analyte Excite, Teledyne Photon Machines) equipped with a double chamber ablation cell (HelEx II) with a single-collector quadrupole ICP-MS (iCAP RQ, Thermo Fisher Scientific). The synthetic USGS basaltic GSD-2 g glass was used as external standard (Wilson, 2018), and ^{29}Si was adopted as internal standard considering the SiO_2 wt% measured with EMPA. A laser fluence of 3.0 J/cm^2 was used with a repetition rate of 10 Hz and the laser spot size was set to 40 μm for all minerals. The Glitter software package (Griffin, 2008) was used for data reduction. The ARM-3 andesitic glass (Wu et al., 2019) and the BCR-2G basaltic glass from the USGS (http://georem.mpch-mainz.gwdg.de) were analyzed together with the unknown as quality control. Precision and accuracy are better than 5 and 10 %, respectively, for most of the elements (Supplementary Table 1).

The *in-situ* B isotope composition of chlorite were measured at the Geochemistry, Geochronology and Isotope Geology Laboratory of the Earth Science Department “A. Desio”, University of Milano LA STATALE (Italy) using a multi-collector (MC-)ICP-MS (Neptune *XT*, Thermo Fisher Scientific) coupled to the laser microprobe system used for trace element determination. Ablation conditions were kept constant between standards and unknown to minimize instrumental isotope fractionation and performed at a repetition rate of 10 Hz, fluence of 3.0 J/cm^2 and in single spot mode with a diameter of 135 μm. The MC-ICP-MS is equipped with highly sensitive X-skimmer and Jet-sample cones and the Jet pump. Boron isotopes were simultaneously collected on two Faraday cups (^{11}B on H4 and ^{10}B on L2) both connected to a 10^{13} Ω resistor amplifiers. This configuration ensures the highest signal/noise ratios, which is mandatory for isotopic determination in minerals with low B contents, such as chlorite. Each analysis consisted of 156 cycles of ~0.5 s each subdivided in 60 cycles of background acquisition, 80 cycles of signal acquisition and 16 cycles of washing time. Data reduction was carried out offline using an *in-house* spreadsheet. A 2SD (standard deviation) outliers test was applied to obtain precise $^{11}B/^{10}B$ ratios. No downhole isotope ratio fractionation was observed. The results are reported in the common delta(δ)-notation as permil (‰) and expressed relative to the isotopic ratio of the NIST SRM951 boric acid ($^{11}B/^{10}B = 4.04362 \pm 0.00137$ 2σ; Catanzaro et al., 1970). Hereafter, uncertainties are reported as 2 standard error (2SE) for single spot analyses and as 2SD for mean values. Quoted uncertainties are quadratic additions of the within run precision of each analysis and the reproducibility of the calibrating standard (which was better than 0.40 ‰). The NIST SRM612 synthetic glass ([B] ~ 34 μg/g, $\delta^{11}B = -0.51 \pm 0.52$ ‰) was used as calibrating standard to account for instrumental and laser-induced isotope fractionation. Due to the lack of suitable reference materials for B isotope determination in chlorite, potential isotope fractionation due to matrix effects were evaluated analyzing a low [B] mylonitic antigorite-bearing serpentinite (sample SY347, [B] ~ 6 μg/g, $\delta^{11}B = +5.62 \pm 0.24$ ‰; H. Marschall, pers. comm.) together with the unknown (Clarke et al., 2020). The measured $\delta^{11}B$ for the SY347 antigorite is $+4.27 \pm 1.92$ ‰ (2σ, $n = 25$, Supplementary Table 2, Supplementary Fig. 3A) and are accurate within uncertainties, suggesting limited matrix effect for serpentine/chlorite minerals with low B contents (see Cannaò et al., 2024 for further information). The estimated mean B content for antigorite-bearing sample SY347 of 6.1 ± 2.2 μg/g (2SD, $n = 25$), overlapping its bulk value.

The *in-situ* Sr isotope compositions of clinopyroxene and epidote were measured at the Geochemistry, Geochronology and Isotope Geology Laboratory of the Earth Science Department “A. Desio”, University of Milano LA STATALE (Italy) using the same LA-MC-ICP-MS instrumentation described above for the $\delta^{11}B$ determination. A spot size from 110 to 65 μm was used, depending on the size of the crystals, with a repetition rate of 10 Hz, fluence of 5.0 J/cm^2 and the He fluxes were set to 0.50 and 0.35 l/min in the sample cell and in the arm of the HelEx II system, respectively. The Sr isotopic data were simultaneous collected in static multicollection mode, using Jet sample and X-skimmer cones to improve instrumental sensitivity. The signal intensities on masses from 82 to 88 (central cup on mass 85) were collected with Faraday cups connected to 10^{11} Ω resistor amplifiers, while half masses of 83.5 and 85.5 were collected with Faraday cups connected to 10^{13} Ω resistor amplifiers. To account for the slow response of the 10^{13} Ω resistors, the tau correction was applied prior to data export as implemented in the MC-ICP-MS software. Each analyses consist of 20 s of background followed by 60 s of signal acquisition employing an integration time of ~0.5 s, for a total of 180 cycles for each analyses. A total of 90–100 cycles were integrated to achieve the final $^{87}Sr/^{86}Sr$ ratios. Data reduction was conducted offline using a modified MS Excel-based spreadsheet from Lugli et al. (2020, version 2). The final $^{87}Sr/^{86}Sr$ ratios are corrected for the potential isobaric contribution of Rb (negligeable in both clinopyroxene and epidote), Kr and the double charged ions of Er and Yb, monitored on half masses 83.5 ($^{167}Er^{2+}$) and 85.5 ($^{171}Yb^{2+}$). The influence of Ca argides and dimers were not considered (see Lugli et al., 2020 for the complete data reduction approach). Reference clinopyroxenes (Zhao et al., 2020) were used to validate the applied method and reported accurate $^{87}Sr/^{86}Sr$ ratios within analytical

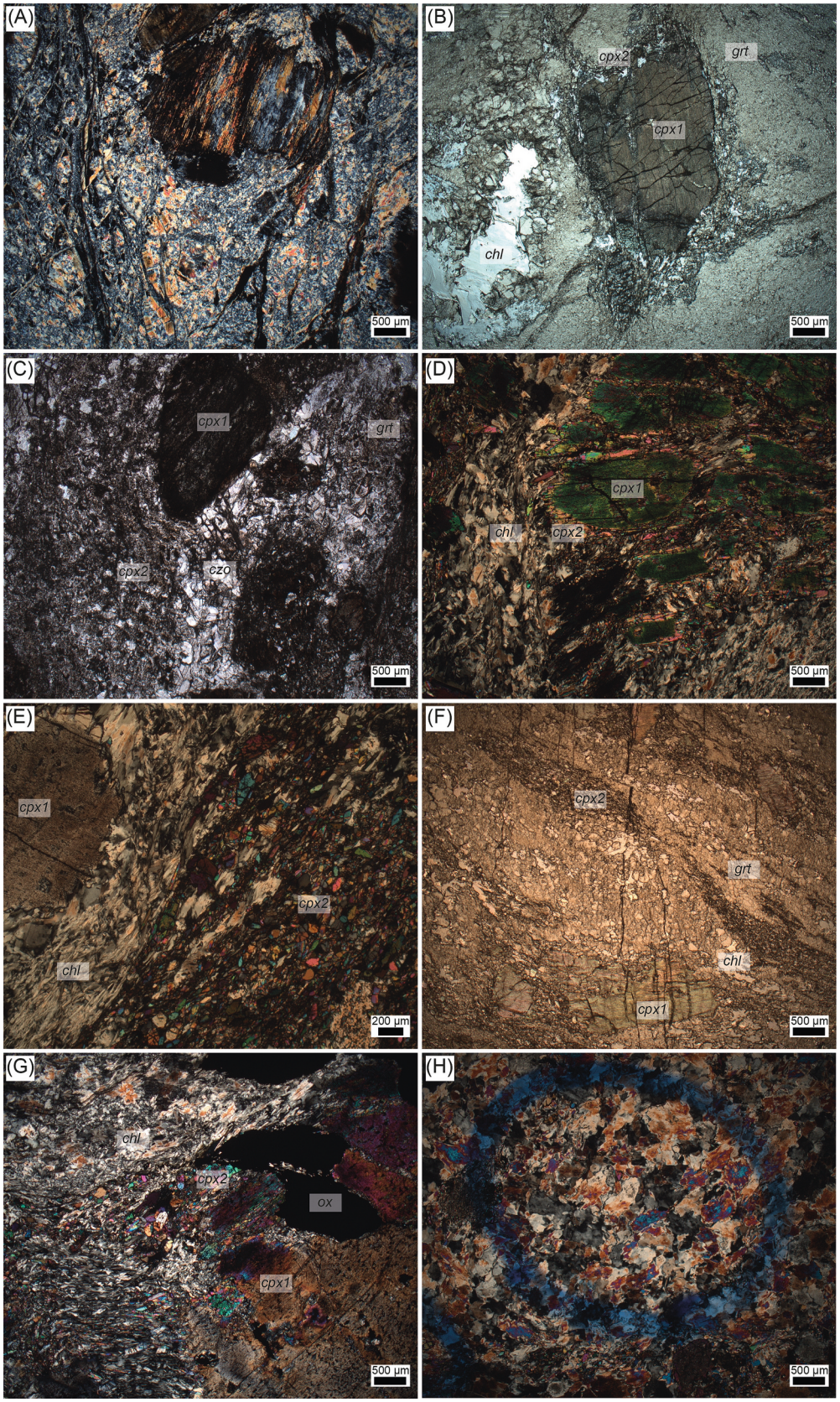

Fig. 2. Microphotographs of key features of the investigated samples. (A) Serpentinized bastite on former pyroxene from sample BCS23–1 surrounded by recrystallized antigorite. Details of the relict igneous clinopyroxene (cpx1, turbid) surrounded by recrystallized clinopyroxene (cpx2, limpid and colourless) from samples BCR21–1B (B), BCR21–2 A (C), BCR23B (D-E), and BCE23 (G). Weak foliation is marked by clinozoisite (czo) and garnet (grt) in sample BCR21–2 A (C), while strong foliation made of chlorite (chl) + cpx2 + grt is displayed in samples BCR23B (E), BCR23A (F), and BCE23 (G). Static recrystallized chlorite from blackwall in sample BCR21–1B is reported in (H).

uncertainties: $^{87}Sr/^{86}Sr = 0.70401 \pm 0.00014$ (2SD, $n = 7$) for YY09–47 and $^{87}Sr/^{86}Sr = 0.70331 \pm 0.00007$ (2SD, n = 2) for YY09–04 (Supplementary Table 3, Supplementary Fig. 3B). Due to the lack of epidote reference materials for *in-situ* Sr isotope analyses, the plagioclase Hrappsay 14–2 (77 % molar anorthite, *ca.* 240 μg/g of Sr) has been analyzed to further check accuracy related to different mineral matrix (Mulder et al., 2023). The measured $^{87}Sr/^{86}Sr$ ratios of 0.70324 ± 0.00018 (2SD, $n = 6$) are accurate within analytical uncertainties with its reference MC-ICP-MS value of 0.703168 ± 0.000018 (2SD; Mulder et al., 2023, Supplementary Table 3, Supplementary Fig. 3B).

4. Results

4.1. Mineral chemistry

Major element compositions of the rock-forming minerals are reported in the Supplementary Table 4. Relicts of preserved igneous clinopyroxene, their recrystallized rims and the second generation of clinopyroxene mostly fall in the diopside field (Fig. 3A; Morimoto et al., 1988). Of relevance is the strong depletion in Al_2O_3 (from 2.9 to 0.02 wt %), FeO_{tot} (from 7.78 to 0.45 wt%) and TiO_2 (from 0.94 to <0.01 wt%) during clinopyroxene recrystallization. Different generations of garnet were identified with composition displaced along the grossular-andradite joint for most of the samples (X_{Grs} = 18.3–96.6 %; Fig. 3B) with a dominant grossular component (mean X_{Grs} = 75.8 %). Andraditic-rich garnets (X_{And} up to 81.7 %) are from the BCE samples, which show high modal amounts of Fe-bearing oxide (Supplementary Fig. S2). Garnet from samples BCE21–1B and BCR21–2 A also show almandine-rich composition (X_{Alm} up to 36.5 %, Fig. 3B). These latter mostly occur within the fine matrix of the metarodingite and are commonly overgrown by X_{Alm}-poor and X_{Grs}-rich garnet (Supplementary Fig. S4). Chlorite from all the samples plot in the clinochlore field (Fig. 3C; Hey, 1954), with no significant difference between chlorite from the host metarodingite and the blackwall. Magnesium value (Mg# = Mg/[Mg + Fe]) in chlorite is variable, ranging from 0.82 in sample BCE21–1B to 0.99 in sample BCR23B. The low Mg# of chlorite from samples BCE likely reflect their high modal amount of Fe-bearing oxide, suggesting that chlorite composition is dependent upon bulk-rock chemistry. Overall, higher Mg# values are documented for chlorite forming the blackwall (Fig. 3C). Clinozoisite from sample BCR 21–2A show low Fe^{3+} contents (from 0.06 to 0.19 apfu). Serpentine has relatively homogenous major element composition independently from texture (bastite, mesh, foliation) and show 42.8 ± 1.2 wt% of SiO_2, 2.0 ± 1.0 wt% of Al_2O_3, 38.3 ± 0.6 wt% of MgO, FeO_{tot} of 2.3 ± 0.3 wt%; it is characterized by high Mg# of 0.97 (± 0.4 RSD%).

4.2. Micro-Raman spectroscopy

Micro-Raman investigations of serpentine in bastite, mesh and foliated texture detect main intensity peaks at *ca.* 227, 376, 684 and 1046 cm^{-1} in the vibration region of the Al—Si network and peaks at *ca.* 3673 and 3702 cm^{-1} in the O—H bond stretching region (Supplementary Fig. S5). These features are discriminatory of the antigorite serpentine polymorph (Auzende et al., 2004; Liu et al., 2023; Petriglieri et al., 2015), particularly the presence of the peak at *ca.* 1046 cm^{-1}, the peak wavenumbers of the bending mode of SiO_4 tetrahedral units, at *ca.* 376, and of the symmetric Si-O-Si stretching mode, at *ca.* 684.

4.3. In-situ trace elements

In-situ trace element concentration of the investigated minerals are reported in the Supplementary Table 4. Relict of igneous clinopyroxene show Rare Earth Element (REE) patterns (Fig. 4a) characterized by depletion in light(L-)REE (La_N/Sm_N = 0.13 to 0.48) and almost flat medium(M-) to heavy(H-)REE (Gd_N/Lu_N = 0.97 to 1.30). A weak negative Eu anomaly is documented (Eu/Eu* down to 0.67), indicating

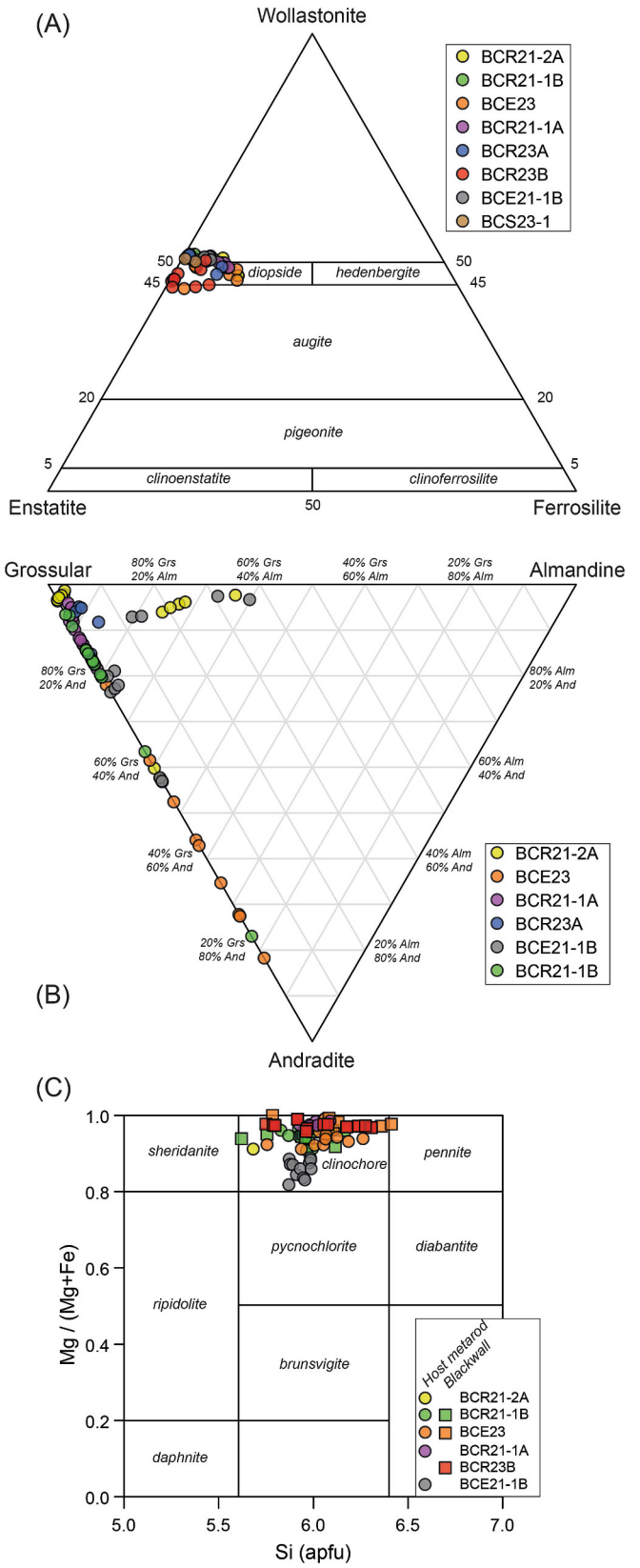

Fig. 3. Classification diagram of (A) clinopyroxene (Morimoto et al., 1988) with all data points falling in the diopside field. Ternary diagrams showing garnet compositions (B). Classification diagrams for chlorite (C) in the Si (apfu) – Mg/(Mg + Fe) space (Hey, 1954).

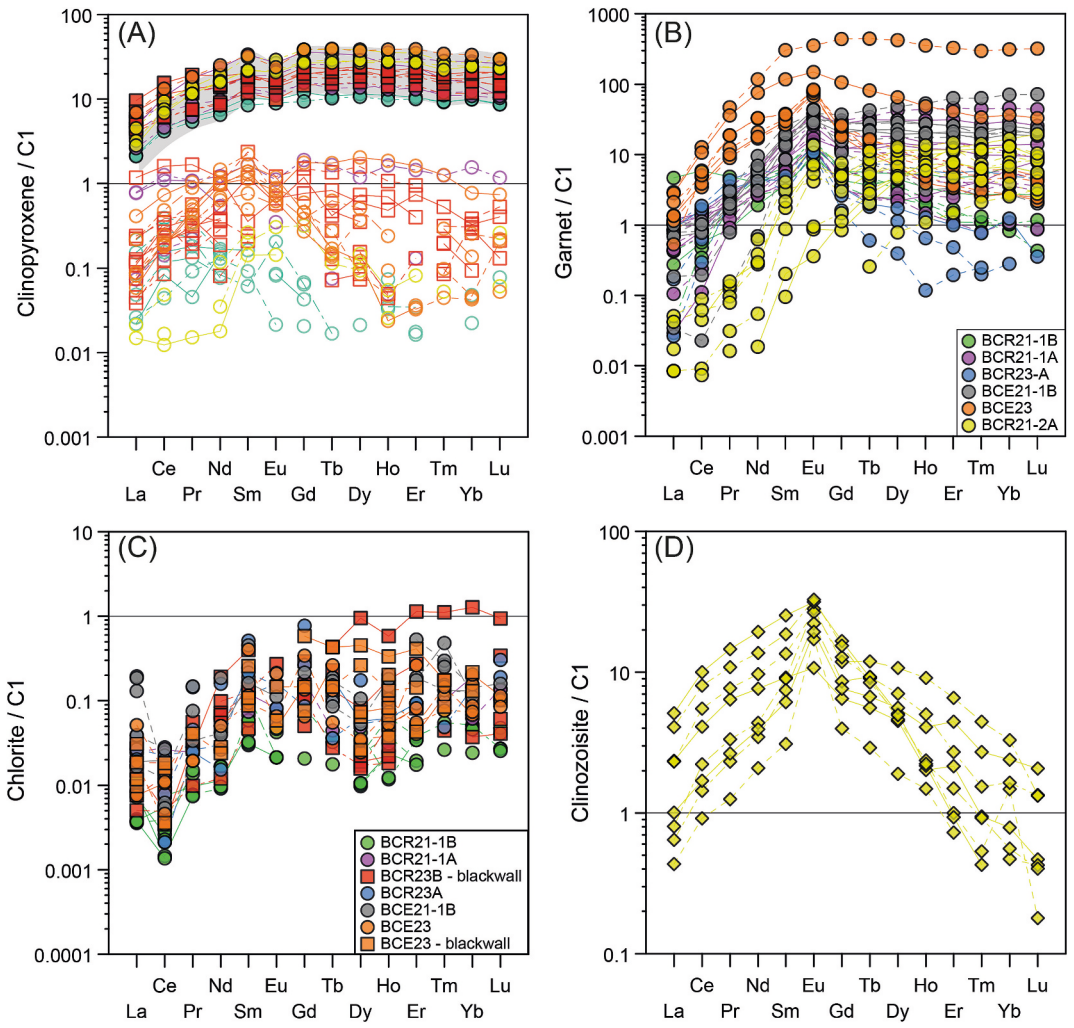

Fig. 4. Chondrite (C1)-normalized REE (McDonough and Sun, 1995) patterns for clinopyroxene (A), garnet (B), chlorite (C) and clinozoiste from sample BCR21–2 A (D). For clinopyroxene, filled symbols refers to igneous porphyroclasts (cpx 1), while open symbol refers to limpid and recrystallized clinopyroxene (cpx 2). Gray field in (A) show the REE variability of igneous clinopyroxene from N. Apennine gabbros (Tribuzio et al., 2014).

equilibrium conditions with igneous plagioclase at magmatic stage(s). By contrast, both recrystallized rims (limpid and colourless, Fig. 2b, d) and metamorphic clinopyroxene (Fig. 2e) show low REE budget (between 2 and 0.01 times the C1 values, Fig. 4a). Garnets mostly show HREE enrichment (Gd_N/Lu_N up to 14.74) and LREE depletion (La_N/Sm_N up to 0.83) with a marked positive Eu anomaly (Eu/Eu* up to 4.90; Fig. 4b). Despite sharing similarities, garnets from different samples show significant REE variability. Of relevance, sample BCR21–2A has the lowest REE budget, with LREE and HREE down to 0.01 and up to 10 times the C1 values, respectively, and limited Eu positive anomaly. From the inner part of the metarodingite BCE23 towards the chlorite blackwall, garnets show the wider REE variability with LREE and HREE decreasing from 10 to 1 and from 600 to 2 times the C1 values, respectively (Fig. 4b). This trend is associated with a pronounced increase of the Eu anomaly (from 1.0 to 3.2). Clinochlore are characterized by very low REE budgets, between 0.001 and 1 times the C1 values and all samples show variably negative Ce anomaly (Fig. 4c). Clinozoisite show convex-REE patterns (Fig. 4d), with a marker depletion in both LREE (La_N/Sm_N = 0.09 to 0.26) and HREE (Gd_N/Lu_N = 6.48 to 38.33), and positive Eu anomaly (Eu_N/Eu_N* up to 4.89).

Magmatic relict of clinopyroxene show positive anomalies in B, Be and Li, and concentrations of Sr, Nd, Zr, Hf, Y and Sc higher than primitive mantle (McDonough and Sun, 1995) values (PM, Fig. 5a). Recrystallized rims of igneous clinopyroxene and clinopyroxene 2 show negative anomalies in Zr and Y and lower Ba, Nd, Hf and Li concentrations with respect to the PM values (Fig. 5a). The depletion in HFSE is mostly related to the loss of TiO_2 during recrystallization. Normalized to PM, garnets mostly show positive anomalies in B, Nd and Y and negative anomaly in Th (Fig. 5b). Clinochlore show positive enrichment in Cs, B, Be and Li from 1 to 30 times the PM values (Fig. 5c). Boron concentration in clinochlore has a mean value of 2.69 ± 0.79 μg/g (1SD) in the rock-suite, while Li shows wide content from 0.930 to 46.0 μg/g, with the highest values pertaining to sample BCE21-1B (27.0 ± 11.7 μg/g, 1SD). Overall, no significant geochemical variation in clinochlore from the host metarodingite and the blackwall is documented. Clinozoisite show positive anomaly in Ba (up to 100 times the primitive mantle values), variable enrichments in Be, Pb and Sr and depletion in HFSE, Th, and U (Fig. 5d).

Overall, antigorite from samples BCS23–1 and 2 show low REE and incompatible trace element budgets (Supplementary Fig. S6). Of relevance, antigorite replacing former pyroxene in bastite texture show low B contents (from 2 to 18 μg/g) compared to foliated antigorite (from 32 to 42 μg/g).

4.4. *In-situ B isotope composition of chlorite*

The B isotope compositions of chlorite in the investigated samples show positive signatures ranging from +6.9 ± 3.2 ‰ to +28.3 ± 1.7 ‰

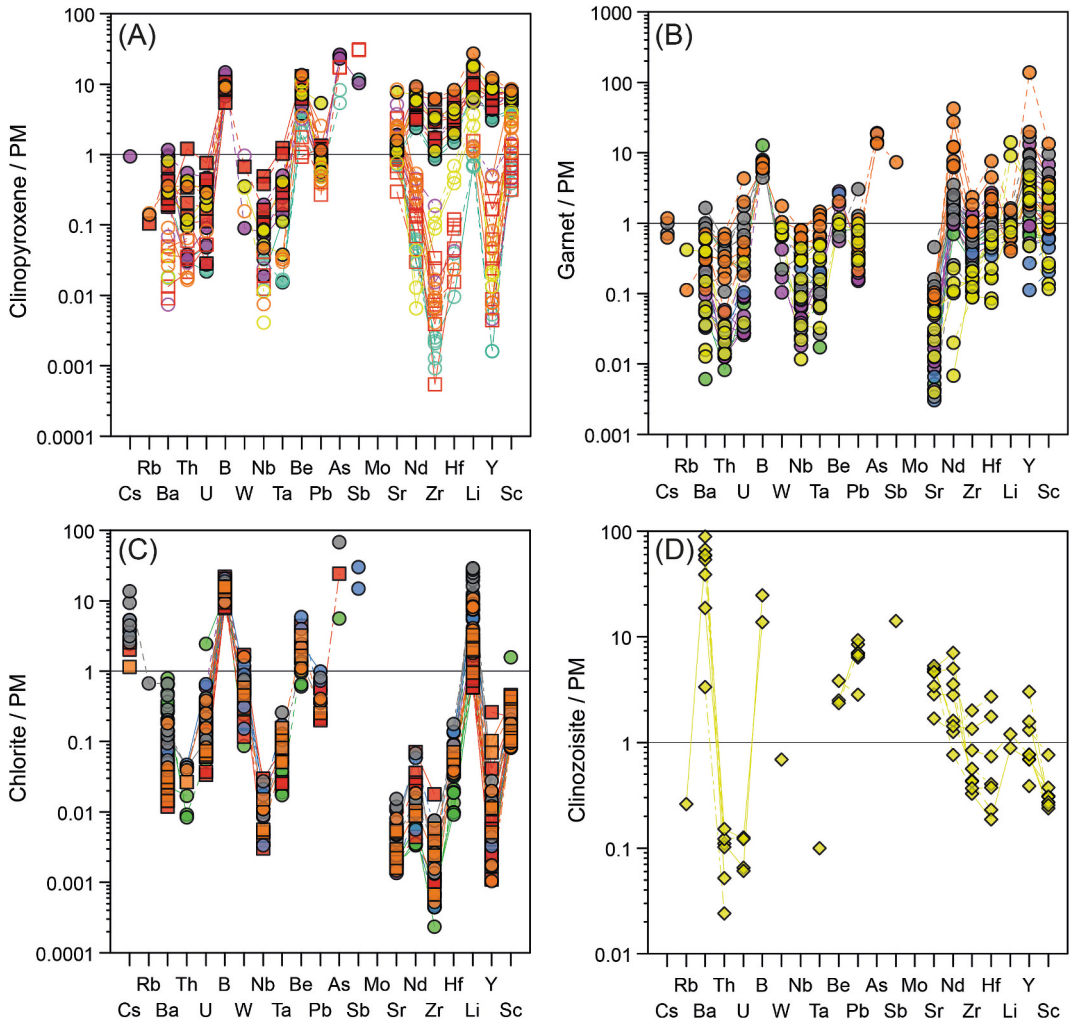

Fig. 5. Primitive mantle (PM)-normalized (McDonough and Sun, 1995) incompatible trace element patterns for clinopyroxene (A), garnet (B), chlorite (C) and clinozoiste (D). Legend as in Fig. 4.

(2SE) for estimated B concentrations ranging between 1.0 and 2.0 μg/g (Table 2). No significant large-scale B-δ^{11}B variation between chlorite of different generations hosted in metarodingites and the chlorite forming the blackwall are documented (Fig. 6a). A certain degree of δ^{11}B variability, however, is still recorded along a profile from the host metarodingite towards the blackwall in sample BCE23. In detail, the δ^{11}B signatures of chlorite show a marked increase from *ca.* +7 to +25 ‰ in the metarodingite ($r^2 = 0.70$) from the core of the body towards the rim that abruptly drops down at *ca.* +15 ‰ within the blackwall (Fig. 7, $r^2 = 0.18$). Several trends are identified within the blackwall of sample BCR23B, in relation to chlorite's microstructure: chlorite close to coarse relict clinopyroxene show high δ^{11}B signatures (up to +25 ‰) compared to foliated chlorite showing lower δ^{11}B imprints (down to +9 ‰). In sample BCR21–1B, chlorite in the metarodingite body show *ca.* 8 ‰ of δ^{11}B variability (from +16.0 ± 2.1 ‰ to +24.6 ± 2.0 ‰, 2SE, $n = 3$), which is overall comparable to the δ^{11}B range shown by the recrystallized chlorite forming the blackwall within uncertainties (from +20.5 ± 2.7 ‰ to +28.3 ± 1.7 ‰, 2SE, $n = 12$; see Table 2).

4.5. *In-situ* $^{87}Sr/^{86}Sr$ *ratios in clinopyroxene and clinozoisite*

The *in-situ* Sr isotope compositions of clinopyroxene and clinozoisite from the investigated samples are reported in Table 3 and Fig. 6B. The Sr isotope composition in the core of the relict clinopyroxene range from 0.70201 ± 0.00071 to 0.70458 ± 0.00027 (2SE) with a mean value of 0.7034 ± 0.0018 (2SD, $n = 10$). The $^{87}Sr/^{86}Sr$ ratios in the recrystallized limpid rims of magmatic pyroxene are identical within errors (from 0.70277 ± 0.00082 to 0.70458 ± 0.00024, 2SE) displaying a mean value of 0.7037 ± 0.0016 (2SD, $n = 5$). Overall, these signatures overlap the Sr isotope compositions of gabbroic rocks from the Ligurian Apennines and Ligurian W. Alps (Cannaò et al., 2023b; Codillo et al., 2022; Schwarzenbach et al., 2021), ranging from 0.70296 to 0.70457, and interpreted to be close to the depleted MORB mantle composition of 0.7025 (Rehkamper and Hofmann, 1997) contaminated by a component related to Jurassic seawater (Schwarzenbach et al., 2021). Metamorphic clinopyroxene (Cpx 2) developed along the metarodingite matrix are characterized by slightly higher $^{87}Sr/^{86}Sr$ ratios ranging from 0.70393 ± 0.00066 to 0.70690 ± 0.00080 (2SE) with a mean value of 0.7051 ± 0.0022 (2SD, $n = 7$). Clinozoisite from sample BCR21–2 A show more radiogenic Sr isotope composition than primary diopside relict, spanning from 0.70528 ± 0.00056 to 0.70666 ± 0.00042 (2SE), with a mean value of 0.7059 ± 0.0011 (2SD, $n = 4$). Overall, the Sr signatures of metamorphic clinopyroxene and clinozoisite trend towards compositions derived from Jurassic seawater (Fig. 6b) of *ca.* 0.7070 (McArthur et al., 2020).

Table 2
In-situ B isotope composition of chlorite.

Sample	# analyses	B (μg/g)	δ^{11}B (‰)	2SE (‰)	Lithology	Texture
BCR23B	C1_chl1	1.6	23.8	2.7	MR	chl2 - foliation
	C1_chl2	1.4	19.6	2.7	MR	chl2 - foliation
	C1_chl3	1.7	16.1	2.3	MR	chl2 - foliation
	C2_chl1	1.6	17.4	2.8	MR	chl1 - coarse
	C2_chl2	1.5	16.6	2.9	MR	chl1 - coarse
	C2_chl3	1.5	9.2	2.6	MR	chl2 - foliation
	C3_chl1	1.6	20.7	2.6	BW	chl2 - massive
	C3_chl2	1.2	20.9	3.2	BW	chl2 - massive
	C3_chl3	1.4	22.5	3.1	BW	chl2 - massive
	C3_chl4	1.4	17.1	2.5	BW	chl2 - massive
	C3_chl5	1.4	14.8	3.2	BW	chl2 - massive
	C3_chl6	1.4	16.0	2.9	BW	chl2 - massive
BCE23	C1_chl1	1.0	6.9	3.2	MR	chl1 - coarse
	C1_chl2	1.1	13.0	4.0	MR	chl1 - coarse
	C1_chl3	1.1	7.5	3.7	MR	chl1 - coarse
	C1_chl4	1.1	11.3	3.7	MR	chl1 - coarse
	L1_chl1	1.1	18.5	4.5	MR	chl1 - coarse
	L1_chl2	1.1	20.5	5.1	MR	chl1 - coarse
	L1_chl3	1.0	26.7	4.4	MR	chl1 - coarse
	L1_chl4	1.0	16.9	3.7	MR	chl1 - coarse
	L1_chl5	1.1	22.4	3.7	MR	chl1 - coarse
	L1_chl6	1.0	25.0	3.6	MR	chl1 - coarse
	L1_chl7	1.1	22.3	4.3	MR	chl1 - coarse
	L1_chl8	1.1	10.1	4.2	BW	chl2 - foliation
	L1_chl9	1.6	13.0	2.2	BW	chl2 - foliation
	L1_chl10	1.5	11.6	2.5	BW	chl2 - foliation
	L1_chl11	1.2	13.9	3.1	BW	chl2 - foliation
	L1_chl12	1.3	18.8	3.3	BW	chl2 - foliation
	L1_chl13	1.6	15.6	2.3	BW	chl2 - foliation
	L1_chl14	1.4	9.5	3.2	BW	chl2 - foliation
	L1_chl15	1.3	16.9	3.5	BW	chl2 - foliation
BCR21–1A	C3_chl2	1.1	23.7	3.6	MR	chl1 - coarse
	C3_chl3	1.2	19.6	3.3	MR	chl1 - coarse
	C3_chl4	1.2	20.7	3.1	MR	chl1 - coarse
BCR21–1B	C3_chl1	1.5	24.5	2.3	BW	chl2 - foliation
	C3_chl2	1.8	20.5	2.7	BW	chl2 - foliation
	C3_chl3	1.9	23.8	1.6	BW	chl2 - foliation
	C3_chl4	1.7	23.5	1.9	BW	chl2 - foliation
	C3_chl5	1.7	22.3	2.0	BW	chl2 - foliation
	C3_chl6	1.8	23.1	1.9	BW	chl2 - foliation
	C3_chl7	1.8	23.8	2.2	BW	chl2 - foliation
	C3_chl8	1.9	26.5	3.0	BW	chl2 - foliation
	C3_chl9	1.8	26.6	1.3	BW	chl2 - foliation
	C4_chl6	1.7	28.3	1.7	MR	chl1 - coarse
	C4_chl7	1.8	26.2	2.0	MR	chl1 - coarse
	C4_chl8	1.9	26.8	1.7	MR	chl1 - coarse
	C2_chl6	1.6	20.4	2.4	MR	chl1 - coarse
	C1_chl6	1.7	24.6	2.0	MR	chl1 - coarse
	C1_chl7	1.7	16.0	2.1	MR	chl1 - coarse

MR: metarodingite; BW: blackwall; B content are estimated with LA-MC-ICP-MS.

5. Discussion

5.1. Oceanic vs. subduction evolution of metarodingite and chlorite blackwall

5.1.1. Pre- to syn-metasomatic evolution of metarodingites

The metarodingite bodies investigated in this study show a dominant mineral assemblage made of clinopyroxene + garnet + chlorite ± epidote, as described for other metarodingites within the Voltri Massif (Cannaò et al., 2023b; Haws et al., 2021; Scambelluri and Rampone, 1999) and Western Alps (Li et al., 2004; Piccoli et al., 2024; Zanoni et al., 2016). This mineral assemblage represents the common paragenesis predicted by modelling to explain rodingite genesis along mafic/ultramafic boundaries by serpentinization fluids at oceanic conditions (Bach and Klein, 2009). The pre-metasomatic history recorded by these rocks derive from the coarse clinopyroxene core, showing REE geochemistry (Fig. 4a) comparable with that of igneous clinopyroxene from the gabbroic sequence of the Jurassic Ligurian ophiolites (Tribuzio et al., 2014) and, for instance, oceanic core complexes of the Mid Atlantic Ridge (Coogan et al., 2000) and Southwest Indian Ridge (Ferrando et al., 2021). The poorly radiogenic $^{87}Sr/^{86}Sr$ isotopic ratios of these igneous clinopyroxene relicts averaging at 0.7034 ± 0.0018 (2SD, n = 10, Fig. 6b) overlap the Sr isotope compositions of gabbroic rocks from the Ligurian Apennines (Schwarzenbach et al., 2021), supporting their dominant record of the pre-metasomatic geochemical imprint of the mantle-derived igneous precursor, partially overprinted by a moderate exchange with Jurassic seawater-derived fluids (Schwarzenbach et al., 2021). The similarity in the Sr isotope ratio between core and rim of igneous clinopyroxene relicts (Fig. 6b) indicates that recrystallization occurred with limited input of external component(s), and to relatively closed-system conditions from oceanic towards subduction evolution. The prominent positive Eu/Eu* anomalies shown by garnet and clinozoisite (Fig. 4b, d), the latter only in sample BCR21–2A, mainly reflect the reaction between primary igneous plagioclase and metasomatic fluid at T between 200 and 300 °C. The association of clinozoisite and garnet,

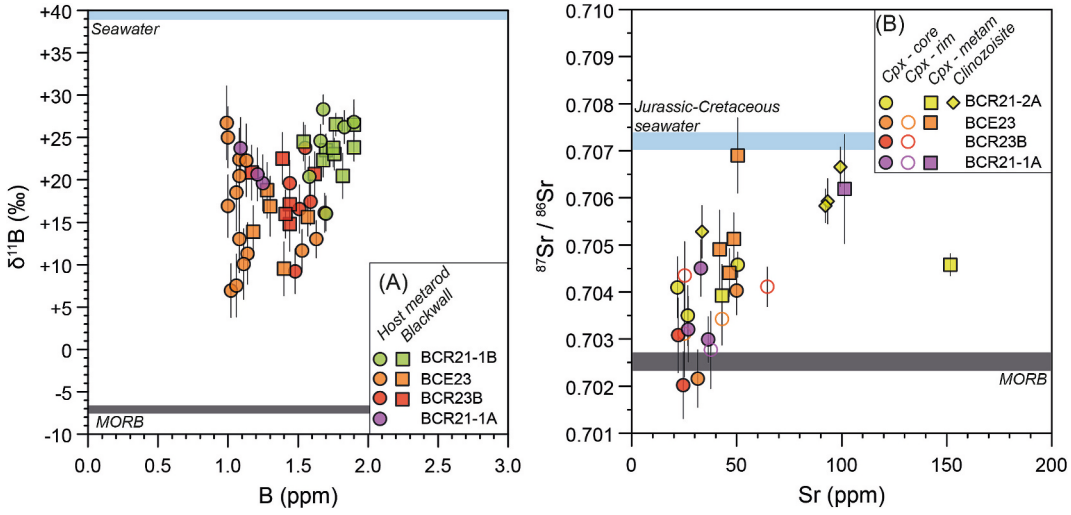

Fig. 6. (A) B (μg/g) *vs.* $\delta^{11}B$ (‰) diagram of chlorite from both metarodingite and blackwall. (B) Sr (μg/g) *vs.* $^{87}Sr/^{86}Sr$ of clinopyroxene (core-rim-metamorphic) and clinozoisite from metarodingite. MORB isotope compositions for B and Sr are from Marschall et al. (2017) and Rehkamper and Hofmann (1997), respectively. Boron isotope seawater composition is from Spivack and Edmond (1987); Jurassic-Cretaceous seawater $^{87}Sr/^{86}Sr$ variability from McArthur et al. (2020).

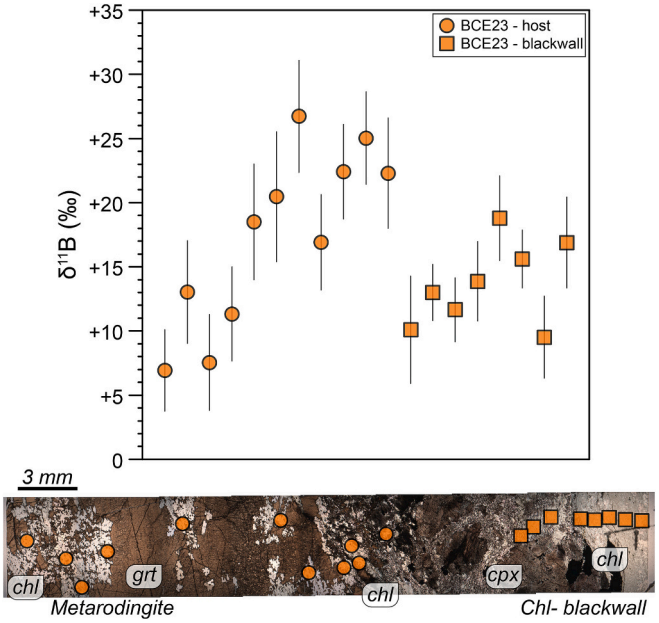

Fig. 7. Profile from metarodingite (circles) to blackwall (squares) showing $\delta^{11}B$ (‰) variability of chlorite along sample BCE23. At the bottom, a microphotograph of the sample profile displays the LA-MC-ICP-MS spot locations.

stable in sample BCR21–2 (Fig. 2c, Supplementary Fig. S4), requires a minimum *T* of 300 °C, relatively high reaction progress and low water/rock (W/R) ratio (Bach and Klein, 2009). The formation of epidote-bearing rodingite should predate the formation of grossular-diopside-bearing rodingite as reaction progress towards higher Ca and Mg enrichments during oceanic metasomatism (Bach and Klein, 2009; Zanoni et al., 2016), although other authors document that epidote-bearing metarodingite may form at high-*P* conditions in response to partial to complete dewatering of the host serpentinites (Laborda-López et al., 2018). The higher variability and radiogenic imprint shown by the $^{87}Sr/^{86}Sr$ isotopic ratios of both clinozoisite and of metamorphic clinopyroxene (cpx2, Fig. 6b) likely reflect the geochemistry of the metasomatic fluids during the rodingitization process, characterized by a pervasive Jurassic seawater-like component. The low REE budget shown by recrystallized clinopyroxene rims in coarse grains (Fig. 4a) and of metamorphic clinopyroxene displaced along the metarodingite foliation (Fig. 2e, f) is associated with the loss of HFSE (Fig. 5a), suggesting their mobilization since the oceanic hydrothermal event(s). The correlation between depletion in HFSE and Ti loss in diopside indicates the dominant role of the clinopyroxene composition (*i.e.*, TiO_2 content) in mobilizing these elements in the hydrous ultramafic-mafic system. The liberated HFSE can be easily redistributed in Ti-bearing accessory minerals (Spandler et al., 2003), such as rutile, ilmenite and titanite, that are common in this petrologic system (Piccoli et al., 2024), or zircon (only during recrystallization at high-*P* conditions). Potentially, HFSE can be also incorporated in Ti-bearing humites in the enclosing serpentinites at both oceanic (*e.g.*, Scambelluri and Rampone, 1999) and subduction (*e.g.*, Garrido et al., 2005) settings. Textural evidence indicates that recrystallization of clinopyroxene 2, displaced along the prograde foliation, is likely associated to the subduction evolution during prograde and/or peak conditions, even though no geochronological constraints are available yet. If a subduction system recrystallization is considered, the trace element and Sr isotope investigations trend towards prograde to peak metamorphic internal recycle and redistribution of elements and isotopic fingerprints initially acquired during the oceanic metasomatic event (Spandler et al., 2003).

5.1.2. Boron isotope systematics and fluid-rock interaction

The high $\delta^{11}B$ imprint shown by chlorite within the metarodingites, dissimilar to the MORB value of −7.1 ± 0.9 ‰ (Marschall et al., 2017), reflects the input of seawater-derived fluid, which is characterized by a ^{11}B-rich signature of +39.5 ‰ (Spivack and Edmond, 1987). The prominent negative Ce anomaly in the C1-normalized REE pattern (Fig. 4c), typical of seawater (Douville et al., 2002), likely supports the formation of chlorite during the oceanic stage. This finding agrees with the Sr isotopic ratios of both clinopyroxene and clinozoisite. The increase in the $\delta^{11}B$ composition shown by chlorite in sample BCE23 as it approaches the blackwall boundary can indeed be used to better unravel B isotope behaviour as rodingitization progresses during the oceanic stage (Fig. 7). Geochemical modelling agrees that rodingitization of mafic bodies is a fluid-driven metasomatic process characterized by steep Si-Ca-activity gradients (Fig. 8) advancing from the contact with the ultramafic rocks into the mafic rocks (Austrheim and Prestvik, 2008; Bach and Klein, 2009; Frost, 1974; Laborda-López et al., 2020, 2018). During this chemical exchange, B is added to the mafic rock leading to a modification of the initial B isotope composition of the MORB-like signature towards higher values (Fig. 8). As reaction progresses, the

Table 3
In-situ Sr isotope composition of clinopyroxene and clinozoisite.

Sample	# analyses	$^{87}Sr/^{86}Sr$	2SE	Sr (V)	$^{85}Rb/^{88}Sr$	Lithology	Mineral	Texture
BCR21–2A	C1_cpx1	0.70458	0.00027	0.56	0.0033	MR	Cpx	Relict igneous core (turbide)
	C1_cpx2	0.70458	0.00024	0.59	0.0032	MR	Cpx	Relict igneous rim (turbide)
	C1_zo4	0.70666	0.00042	0.34	0.0245	MR	Czo	Czo dispaced along foliation
	C1_zo5	0.70528	0.00056	0.23	0.0006	MR	Czo	Czo dispaced along foliation
	C1_zo6	0.70593	0.00048	0.26	<0.0001	MR	Czo	Czo dispaced along foliation
	C2_cpx1	0.70350	0.00064	0.24	0.0021	MR	Cpx	Relict igneous core
	C2_cpx2	0.70410	0.00065	0.25	0.0023	MR	Cpx	Relict igneous core
	C2_zo3	0.70583	0.00036	0.42	<0.0001	MR	Czo	Czo dispaced along foliation
BCE23	C1_cpx1	0.70271	0.00080	0.25	<0.0001	MR	Cpx	Relict igneous core (turbide)
	C1_cpx5c	0.70216	0.00061	0.22	<0.0001	MR	Cpx	Relict igneous core (turbide)
	C1_cpx5r	0.70312	0.00093	0.16	<0.0001	MR	Cpx	Relict igneous rim (turbide)
	L1_cpx-c	0.70403	0.00051	0.27	<0.0001	MR	Cpx	Metamorphic cpx
	L1_cpx-r	0.70343	0.00056	0.25	<0.0001	MR	Cpx	Metamorphic cpx
	L1_cpx4	0.70441	0.00051	0.30	<0.0001	MR	Cpx	Metamorphic cpx
	L1_cpx2	0.70513	0.00055	0.25	<0.0001	MR	Cpx	Metamorphic cpx
BCR23B	C1_cpx1	0.70202	0.00071	0.16	0.0008	MR	Cpx	Relict igneous core (turbide)
	C1_cpx2	0.70435	0.00072	0.17	<0.0001	MR	Cpx	Relict igneous rim (turbide)
	C2_cpx1	0.70308	0.00080	0.16	0.0008	MR	Cpx	Relict igneous core
	C2_cpx2	0.70411	0.00042	0.32	0.0010	MR	Cpx	Relict igneous rim (limpid)
BCR21–1A	C1_cpx1	0.70451	0.00060	0.22	0.0010	MR	Cpx	Relict igneous core (turbide)
	C1_cpx2	0.70321	0.00070	0.20	<0.0001	MR	Cpx	Relict igneous core (turbide)
	C1_cpx3	0.70619	0.00116	0.10	<0.0001	MR	Cpx	Metamorphic cpx
	C2_cpx1	0.70299	0.00049	0.25	0.0005	MR	Cpx	Relict igneous core (turbide)
	C2_cpx2	0.70277	0.00082	0.22	0.0029	MR	Cpx	Relict igneous rim (turbide)

MR: metarodingite; Cpx and Czo refer to clinopyroxene and clinozoisite, respectively.

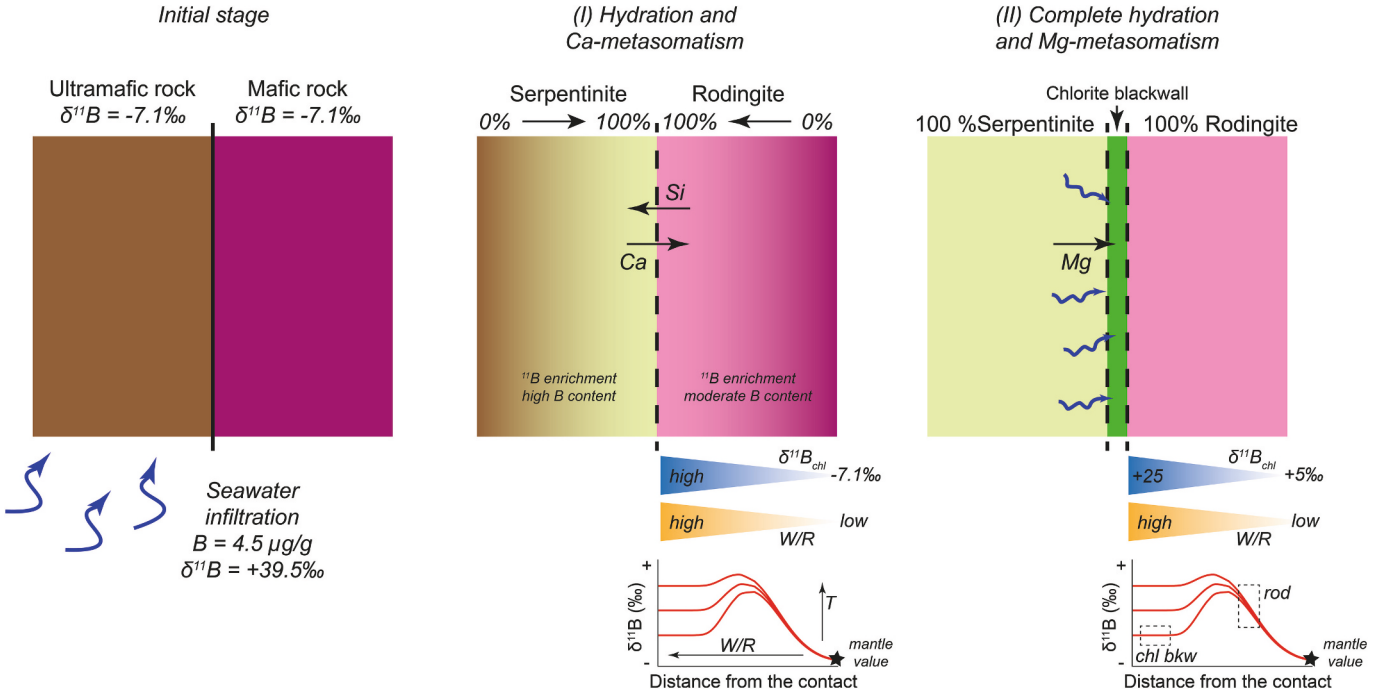

Fig. 8. Schematic representation of $\delta^{11}B$ variation along the ultramafic/mafic contact during rodingitization process caused by seawater infiltration. During the first stage of hydration and Ca-metasomatism (I), the mafic rock acquires variable B content and a ^{11}B-enriched isotope composition depending on W/R ratios and *T* conditions of the system. The W/R ratio influences the $\delta^{11}B$ variability of the newly-formed rodingite as a function of the distance from the ultramafic/mafic contact, as schematically illustrated at the bottom of the sketch. The *T* further impacts the final B isotope composition of the rodingite by controlling the B isotope fractionation between fluid and minerals. As reaction progress, complete hydration of the ultramafic/mafic system and the development of the chlorite blackwall associated to Mg-metasomatism (II) strongly modify the initial $\delta^{11}B$ composition of the mafic protolith, shifting it towards positive values in both rodingite and blackwall, as also shown schematically at the bottom of the sketch. These qualitative diagrams illustrate the spatial trends in $\delta^{11}B$ and W/R ratios across the contact, with $\delta^{11}B$ profiles showing enrichment relative to mantle values and peaking near the blackwall-rodingite interface. Red lines represent trend variations at different *T*. (For interpretation of the references to colour in this figure legend, the reader is referred to the web version of this article.)

W/R ratio generally increases along the contact with the serpentinized ultramafic host compared to the core of the metasomatized mafic body (Bach and Klein, 2009). In the past years several modelling attempts have been done to unravel how W/R ratio may control the B isotope composition in ultramafic systems (*e.g.*, Cannaò and Debret, 2024; Prigent et al., 2018), and results overall agree to a general increase of the $\delta^{11}B$ imprint of the hydrous minerals with the increase of the W/R ratio of the system at the beginning of the process. This behaviour can reasonably explain the B isotopic signatures of chlorite displaced along the profile documented in BCE23 (Fig. 7), as schematically illustrated in Fig. 8. As long as the gradient in the W/R ratio is present, chlorite in the host metarodingite is able to record different $\delta^{11}B$ signatures. The lack of clear trends in the $\delta^{11}B$ values measured for the other metarodingite bodies (*e.g.*, BCR21–1) can conceivably be explained by considering a relatively steady W/R ratio condition associated with the rodingitization process at the oceanic stage. The more homogeneous $\delta^{11}B$ imprints of these rocks may also reflect a pronounced Ca-metasomatism affecting these mafic bodies compared to BCE samples. In fact, sample BCE21-1, showing higher modal amounts of oxides (Fig. 1d, Supplementary Fig. 2) due to a more differentiated mafic protolith, indicates indeed that the magmatic history of mafic bodies prior to oceanic alteration may also influence their ability to acquire variable $\delta^{11}B$ imprints (*e.g.*, Cannaò et al., 2023b). The development of the chlorite blackwall along the contact between metarodingite and serpentinites (Fig. 1) exhibits more homogeneous $\delta^{11}B$ signatures (sample BCE23), likely reflecting a higher W/R ratio associated with Mg-metasomatism (Figs. 7, 8), following the rodingitization process. Such a chlorite-rich layer can form either during the oceanic stage (*e.g.*, Barriga and Fyfe, 1983; Dubińska et al., 2004) or during subduction zone metamorphism (*e.g.*, Piccoli et al., 2024; Shen et al., 2016), the latter as the results of high fluid flux driven by Mg-rich aqueous fluid derived from the surrounding dehydrating serpentinites. The intense metasomatic modification of both metarodingite and chlorite blackwall associated with fluid-rock interaction processes is also recorded by the extremely low $\delta^{26}Mg$ isotope shown by these lithologies exposed in the Voltri Massif (Xiong et al., 2024). Based on data presented in this study and the lack of detailed geochronological information, the development of chlorite-blackwall is interpreted to derive from the oceanic alteration stage. To date, there are no strong arguments supporting a clear development of the chlorite blackwall during prograde subduction processes, although blackwall foliation is consistent with the prograde foliation in serpentinite overgrown by high-*P* olivine veins (Fig. 1a, d). Considering the ^{11}B-enrichment of serpentinite-derived fluids at high-*P* (Cannaò, 2020; Li et al., 2022), the formation of chlorite blackwall during prograde to peak metamorphism is expected to be enriched in ^{11}B, likely overlapping the oceanic signatures. Currently, further investigations aimed to better unravel the B partitioning between chlorite and fluids are difficult due to the lack of information on the B behaviour in chlorite during rodingitization and, more importantly, B isotope fractionation between chlorite and fluids. Specific works are required to address these open questions.

5.2. Implications for deep B recycling

Chlorite is an important mineral in mafic-ultramafic systems due to its wide stability at high-*P* (Pawley, 2003), allowing it to transport significant amounts of aqueous fluids beyond arc depths. Its behaviour in subduction zones has recently been revisited, particularly in chlorite-rich metasomatic rocks, with particular attention to its destabilization at *UHP* conditions. This destabilization leads to the formation of DHMSs, such as 11.5 Å and Mg-sursassite (Hermann and Lakey, 2021). These phase transitions have been identified as an unaccounted reservoir governing the deep-water cycle on geological timescale. Despite its importance, geochemical information about chlorite in high-*P* regimes is poorly known (Marschall et al., 2006), particular with reference to its B isotope inventory. Similarly, the geochemical behaviour of B and other incompatible elements in chlorite-related DHMSs is still largely unconstrained (Cannaò et al., 2023a). The geochemical results presented in this study indicate that, although chlorite hosts less B compared to the surrounding antigorite-bearing serpentinites, its B content is still several orders of magnitude higher than that of depleted mantle values (Marschall et al., 2017). Furthermore, the B isotopic signature of chlorite in metarodingites is enriched in the heavy ^{11}B isotope, with $\delta^{11}B$ signatures 15 to 30 ‰ higher than the mantle baseline. This evidence suggests that chlorite destabilization could reasonably release ^{11}B-rich fluids beyond sub-arc depths.

Chlorite-rich mélanges in subduction zones commonly form through intense metasomatic reactions induced by slab-derived fluids migrating along the slab–mantle interface (Bebout and Penniston-Dorland, 2016). These hydrous fluids, released during progressive dehydration of the subducting oceanic crust and sediments (Hacker, 2008), react with overlying ultramafic and mafic rocks, stabilizing chlorite and other hydrous minerals such as amphibole and talc under high-*P* conditions (Codillo et al., 2022; Easthouse et al., 2025; Marschall and Schumacher, 2012; Spandler et al., 2008; Xiong et al., 2024). The resulting chlorite-bearing mélange domains serve as major fluid conduits and mechanical decoupling horizons, playing a critical role in element transport, deformation localization, and the geochemical evolution of the mantle wedge (Bebout and Barton, 2002; Cannaò and Malaspina, 2018; Hoover et al., 2022; Spandler and Pirard, 2013). From a B isotope perspective, the B isotope composition in such chlorite-rich mélange can be strongly influenced by fluid-rock chemical exchanges. This isotopic modification reflects the extent of fluid infiltration and metasomatic overprinting, providing key insights into the timing, source, and pathways of slab-derived fluid migrating along the subduction interface, with important implications for B recycling both at volcanic arcs and in deeper mantle region(s).

6. Conclusions

This work presents new geochemical data on chlorite from an association of metarodingite and blackwall developed along the contact between metarodingite and high-*P* serpentinites from the Voltri Massif in the Western Ligurian Alps (Italy). The main point of this contribution can be summarized as follows: (i) the metarodingite bodies exhibit a common assemblage of clinopyroxene + garnet + chlorite ± epidote, consistent with rodingitization along mafic/ultramafic boundaries at oceanic conditions. *In-situ* $^{87}Sr/^{86}Sr$ ratios and REE signatures of igneous clinopyroxene cores indicate preservation of pre-metasomatic mantle-derived geochemistry, with limited overprinting by seawater-derived fluids; (ii) the $\delta^{11}B$ values documented in chlorite vary across samples and spatially within metarodingites, reflecting gradients in W/R ratio and the influence of seawater-derived B-rich fluids during oceanic alteration. The chlorite-blackwall layers display more homogeneous $\delta^{11}B$ signatures, likely due to Mg-metasomatism and high W/R conditions at the mafic-ultramafic interface. Whether this signature was inherited from the oceanic stage or development during prograde subduction remains unresolved; (iii) metamorphic clinopyroxene and clinozoisite show evidence of trace element redistribution (*e.g.*, HFSE loss, positive Eu anomalies), likely due to prograde metamorphism during subduction. However, Sr isotopes largely reflect oceanic-stage metasomatism, suggesting a closed-system evolution with limited input of external fluids during subduction; (iv) chlorite destabilization at high-*P* conditions could release ^{11}B-rich fluids, while its B isotope composition in mélange zones – shaped by fluid–rock exchange – might provide critical insights into deep fluid pathways and B recycling from arcs to the deeper mantle.

CRediT authorship contribution statement

E. Cannaò: Writing – review & editing, Writing – original draft, Visualization, Validation, Supervision, Resources, Project administration, Methodology, Investigation, Funding acquisition, Formal analysis,

Data curation, Conceptualization.

Declaration of competing interest

The authors declare that they have no known competing financial interests or personal relationships that could have appeared to influence the work reported in this paper.

Acknowledgements

This work benefit funding from the Italian Ministry of University and Research (MUR) – Excellent Departments Projects 2018-2022 and 2023-2027– and Università degli Studi di Milano through "Piano di Sostegno alla Ricerca: linea 2, anno 2025". Gianluca Sessa (University of Milano, Italy) is thanked for support during the micro-analytical sessions, Marco Scambelluri is acknowledged for the full access to the Micro-Raman facility at the University of Genova (Italy). Laura Crispini and Donato Belmonte (University of Genova) are acknowledged for stimulating discussion about the area. Constructive reviews by Yi-Xiang Chen and an anonymous referee, and editorial handling by Co-Editor-in-Chief Marco Fiorentini, improved the manuscript and are much appreciated. Open access publishing facilitated by università degli Studi di Milano, as part of the Elsevier - CRUI-CARE agreement.

Appendix A. Supplementary data

Supplementary data to this article can be found online at https://doi.org/10.1016/j.chemgeo.2025.123125.

Data availability

All data used in this contribution are available in the main text or in the supplementary files

References

Austrheim, H., Prestvik, T., 2008. Rodingitization and hydration of the oceanic lithosphere as developed in the Leka ophiolite, north-central Norway. Lithos 104, 177–198. https://doi.org/10.1016/j.lithos.2007.12.006.

Auzende, A.L., Daniel, I., Reynard, B., Lemaire, C., Guyot, F., 2004. High-pressure behaviour of serpentine minerals: a Raman spectroscopic study. Phys. Chem. Miner. 31, 269–277. https://doi.org/10.1007/s00269-004-0384-0.

Bach, W., Klein, F., 2009. The petrology of seafloor rodingites: insights from geochemical reaction path modeling. Lithos 112, 103–117. https://doi.org/10.1016/j.lithos.2008.10.022.

Bach, W., Jöns, N., Klein, F., 2013. Metasomatism Within the Ocean Crust, pp. 253–288. https://doi.org/10.1007/978-3-642-28394-9_8.

Barriga, F., Fyfe, W.S., 1983. Development of rodingite in basaltic rocks in serpentinites, East Liguria, Italy. Contrib. Mineral. Petrol. 84, 146.

Bebout, G.E., 2013. Metasomatism in Subduction Zones of Subducted Oceanic Slabs, Mantle Wedges, and the Slab-Mantle Interface, pp. 289–349. https://doi.org/10.1007/978-3-642-28394-9_9.

Bebout, G.E., Barton, M.D., 2002. Tectonic and metasomatic mixing in a high-T, subduction-zone mélange—insights into the geochemical evolution of the slab–mantle interface. Chem. Geol. 187, 79–106. https://doi.org/10.1016/S0009-2541(02)00019-0.

Bebout, G.E., Penniston-Dorland, S.C., 2016. Fluid and mass transfer at subduction interfaces-the field metamorphic record. Lithos. https://doi.org/10.1016/j.lithos.2015.10.007.

Bekaert, D.V., Turner, S.J., Broadley, M.W., Barnes, J.D., Halldórsson, S.A., Labidi, J., Wade, J., Walowski, K.J., Barry, P.H., 2021. Subduction-Driven Volatile Recycling: A Global Mass Balance. The Annual Review of Earth and Planetary Sciences is online at earth.annualreviews.org, 49, pp. 37–70. https://doi.org/10.1146/annurev-earth-071620.

Cannaò, E., 2020. Boron isotope fractionation in subducted serpentinites: a modelling attempt. Lithos 376–377. https://doi.org/10.1016/j.lithos.2020.105768.

Cannaò, E., 2025. Subducted ophicarbonates as source for B-bearing diamond formation. Chem. Geol. 680. https://doi.org/10.1016/j.chemgeo.2025.122693.

Cannaò, E., Debret, B., 2024. Variable δ11B signatures reflect dynamic evolution of the Mariana serpentinite forearc. Geochem. Perspect. Lett. 30, 13–19. https://doi.org/10.7185/geochemlet.2416.

Cannaò, E., Malaspina, N., 2018. From oceanic to continental subduction: implications for the geochemical and redox evolution of the supra-subduction mantle. Geosphere 14. https://doi.org/10.1130/GES01597.1.

Cannaò, E., Scambelluri, M., Agostini, S., Tonarini, S., Godard, M., 2016. Linking serpentinite geochemistry with tectonic evolution at the subduction plate-interface: the Voltri Massif case study (Ligurian Western Alps, Italy). Geochim. Cosmochim. Acta 190, 115–133. https://doi.org/10.1016/j.gca.2016.06.034.

Cannaò, E., Milani, S., Merlini, M., Tiepolo, M., Fumagalli, P., 2023a. Phase-a as boron carrier in the Earth's interior. Lithos 452–453, 107211. https://doi.org/10.1016/j.lithos.2023.107211.

Cannaò, E., Scambelluri, M., Müntener, O., Putlitz, B., Agostini, S., 2023b. Inheritance versus subduction-related δ11B signatures of eclogites: insights from the Voltri Massif (Ligurian Western Alps, Italy). Chem. Geol. 615, 121218. https://doi.org/10.1016/j.chemgeo.2022.121218.

Cannaò, E., Tiepolo, M., Agostini, S., Scambelluri, M., 2024. Fossil hydrothermal oceanic systems through in-situ B isotopes in ophicarbonates (N. Apennines, Italy). Chem. Geol. 645. https://doi.org/10.1016/j.chemgeo.2023.121899.

Capponi, G., Crispini, L., Federico, L., Malatesta, C., 2016. Geology of the eastern ligurian alps: a review of the tectonic units. Ital. J. Geosci. 135, 157–169. https://doi.org/10.3301/IJG.2015.06.

Catanzaro, E.J., Champion, C.E., Garner, E.L., Marinenko, G., Sappenfield, K.M., Shields, W.R., 1970. Boric Acid: isotopic and assay standard reference materials. Natl. Bureau Stand. Instit. Mater. Res. 260, 1–70.

Clarke, E., de Hoog, J.C.M., Kirstein, L.A., Harvey, J., Debret, B., 2020. Metamorphic olivine records external fluid infiltration during serpentinite dehydration. Geochem. Perspect. Lett. 16, 25–29. https://doi.org/10.7185/GEOCHEMLET.2039.

Codillo, E.A., Klein, F., Dragovic, B., Marschall, H.R., Baxter, E., Scambelluri, M., Schwarzenbach, E., 2022. Fluid-mediated mass transfer between mafic and ultramafic rocks in subduction zones. Geochem. Geophys. Geosyst. 23. https://doi.org/10.1029/2021GC010206.

Coogan, L.A., Saunders, A.D., Kempton, P.D., Norry, M.J., 2000. Evidence from oceanic gabbros for porous melt migration within a crystal mush beneath the Mid-Atlantic Ridge. Geochem. Geophys. Geosyst. 1. https://doi.org/10.1029/2000GC000072.

De Hoog, J.C.M., Savov, I.P., 2018. Boron isotopes as a tracer of subduction zone processes. In: Horst, M., Foster, G. (Eds.), Boron Isotopes: The Fifth Element. Springer International Publishing, Cham, pp. 217–247. https://doi.org/10.1007/978-3-319-64666-4_9.

Douville, E., Charlou, J.L., Oelkers, E.H., Bienvenu, P., Colon, C.F.J., Donval, J.P., Fouquet, Y., Prieur, D., Appriou, P., 2002. The rainbow vent fluids (36°14VN, MAR): the influence of ultramafic rocks and phase separation on trace metal content in Mid-Atlantic Ridge hydrothermal fluids. Chem. Geol. 184, 38–48.

Dubińska, E., Bylina, P., Kozłowski, A., Dörr, W., Nejbert, K., Schastok, J., Kulicki, C., 2004. U-Pb dating of serpentinization: hydrothermal zircon from a metasomatic rodingite shell (Sudetic ophiolite, SW Poland). Chem. Geol. 203, 183–203. https://doi.org/10.1016/j.chemgeo.2003.10.005.

Easthouse, G., Hoover, W., Teng, F.Z., Condit, C., Pike, C., Wang, Z.Z., Berg, A., Wynn, P., Woods, L., Poulaki, E., 2025. Formation of talc in the subduction interface: Mg isotopes demonstrate Mg loss over Si gain. Geology 53, 398–403. https://doi.org/10.1130/G52538.1.

Federico, L., Crispini, L., Scambelluri, M., Capponi, G., 2007. Ophiolite mélange zone records exhumation in a fossil subduction channel. Geology 35, 499–502. https://doi.org/10.1130/G23190A.1.

Ferrando, C., France, L., Basch, V., Sanfilippo, A., Tribuzio, R., Boulanger, M., 2021. Grain size variations record segregation of residual melts in slow-spreading oceanic crust (Atlantis Bank, 57°E Southwest Indian Ridge). J. Geophys. Res. Solid Earth 126. https://doi.org/10.1029/2020JB020997.

Frost, B.R., 1974. Contact metamorphism of serpentinite, chloritic blackwall and rodingite at Paddy-Go-Easy Pass, Central Cascades, Washington. J. Petrol. 2, 272–313.

Garrido, C.J., Sánchez-Vizcaíno, V.L., Gómez-Pugnaire, M.T., Trommsdorff, V., Alard, O., Bodinier, J.L., Godard, M., 2005. Enrichment of HFSE in chlorite-harzburgite produced by high-pressure dehydration of antigorite-serpentinite: implications for subduction magmatism. Geochem. Geophys. Geosyst. 6. https://doi.org/10.1029/2004GC000791.

Griffin, W.L., 2008. GLITTER: data reduction software for laser ablation ICP-MS. In: Laser Ablation ICP-MS in the Earth Sciences: Current Practices and Outstanding Issues, pp. 308–311.

Hacker, B.R., 2008. H2O subduction beyond arcs. Geochem. Geophys. Geosyst. 9. https://doi.org/10.1029/2007GC001707.

Halama, R., Konrad-Schmolke, M., De Hoog, J.C.M., 2020. Boron isotope record of peak metamorphic ultrahigh-pressure and retrograde fluid–rock interaction in white mica (Lago di Cignana, Western Alps). Contrib. Mineral. Petrol. 175. https://doi.org/10.1007/s00410-020-1661-8.

Haws, A.A., Starr, P.G., Dragovic, B., Scambelluri, M., Belmonte, D., Caddick, M.J., Broadwell, K.S., Ague, J.J., Baxter, E.F., 2021. Meta-rodingite dikes as recorders of subduction zone metamorphism and serpentinite dehydration: Voltri Ophiolite, Italy. Chem Geol 565. https://doi.org/10.1016/j.chemgeo.2021.120077.

Hermann, J., Lakey, S., 2021. Water transfer to the deep mantle through hydrous, Al-rich silicates in subduction zones. Geology 49, 911–915. https://doi.org/10.1130/G48658.1.

Hey, M.H., 1954. A new review of the chlorites. Mineral. Mag. J. Mineral. Soc. 30, 277–292. https://doi.org/10.1180/minmag.1954.030.224.01.

Hoover, W.F., Condit, C.B., Lindquist, P.C., Moser, A.C., Guevara, V.E., 2022. Episodic slow slip hosted by talc-bearing metasomatic rocks: high strain rates and stress amplification in a chemically reacting shear zone. Geophys. Res. Lett. 49. https://doi.org/10.1029/2022GL101083.

Irifune, T., Kubo, N., Isshiki, M., Yamasaki, Y., 1998. Phase transformations in serpentine and transportation of water into the lower mantle. Geophys. Res. Lett. 25, 203–206. https://doi.org/10.1029/97GL03572.

Ishikawa, T., Nakamura, E., 1993. Boron isotope systematics of marine sediments. Earth Planet. Sci. 117 (3–4), 567–580.
Iwamori, H., 2004. Phase relations of peridotites under H2O-saturated conditions and ability of subducting plates for transportation of H2O. Earth Planet. Sci. Lett. 227, 57–71. https://doi.org/10.1016/j.epsl.2004.08.013.
Konrad-Schmolke, M., Halama, R., 2014. Combined thermodynamic–geochemical modeling in metamorphic geology: boron as tracer of fluid–rock interaction. Lithos 208–209, 393–414. https://doi.org/10.1016/j.lithos.2014.09.021.
Kowalski, P.M., Wunder, B., 2018. Boron Isotope Fractionation among Vapor–Liquids–Solids–Melts: experiments and Atomistic Modeling, pp. 33–69. https://doi.org/10.1007/978-3-319-64666-4_3.
Laborda-López, C., López-Sánchez-Vizcaíno, V., Marchesi, C., Gómez-Pugnaire, M.T., Garrido, C.J., Jabaloy-Sánchez, A., Padrón-Navarta, J.A., Hidas, K., 2018. High-P metamorphism of rodingites during serpentinite dehydration (Cerro del Almirez, Southern Spain): implications for the redox state in subduction zones. J. Metam. Geol. 36, 1141–1173. https://doi.org/10.1111/jmg.12440.
Laborda-López, C., Marchesi, C., López Sánchez-Vizcaíno, V., Gómez-Pugnaire, M.T., Dale, C.W., Jabaloy-Sánchez, A., Padrón-Navarta, J.A., Román-Alpiste, M.J., Garrido, C.J., 2020. Geochemical evolution of rodingites during subduction: insights from Cerro del Almirez (southern Spain). Lithos 370–371. https://doi.org/10.1016/j.lithos.2020.105639.
Li, X.P., Rahn, M., Bucher, K., 2004. Metamorphic processes in rodingites of the zermatt-saas ophiolites. Int. Geol. Rev. 46, 28–51. https://doi.org/10.2747/0020-6814.46.1.28.
Li, Y.C., Wei, H.Z., Palmer, M.R., Ma, J., Jiang, S.Y., Chen, Y.X., Lu, J.J., Liu, X., 2022. Equilibrium boron isotope fractionation during serpentinization and applications in understanding subduction zone processes. Chem. Geol. 609. https://doi.org/10.1016/j.chemgeo.2022.121047.
Liu, X., Ma, Y., Yan, W., He, M., Li, L., Sui, X., Peng, B., 2023. Identify key serpentines antigorite, lizardite and chrysotile with various compositions and crystallographic orientations using micro-Raman spectroscopy. Solid Earth Sci. 8, 295–304. https://doi.org/10.1016/j.sesci.2023.10.003.
Lugli, F., Weber, M., Giovanardi, T., Arrighi, S., Bortolini, E., Figus, C., Marciani, G., Oxilio, G., Romandini, M., Silvestrini, S., Jochum, K.P., Benazzi, S., Cipriani, A., 2020. Fast offline data reduction of laser ablation MC-ICP-MS Sr isotope measurements: via an interactive Excel-based spreadsheet "SrDr. J. Anal., At. Spectrom. 35, 852–862. https://doi.org/10.1039/c9ja00424f.
Malatesta, C., Crispini, L., Federico, L., Capponi, G., Scambelluri, M., 2012. The exhumation of high pressure ophiolites (Voltri Massif, Western Alps): insights from structural and petrologic data on metagabbro bodies. Tectonophysics 568–569, 102–123. https://doi.org/10.1016/j.tecto.2011.08.024.
Marschall, H.R., Schumacher, J.C., 2012. Arc magmas sourced from mélange diapirs in subduction zones. Nat. Geosci. https://doi.org/10.1038/ngeo1634.
Marschall, H.R., Altherr, R., Ludwig, T., Kalt, A., Gméling, K., Kasztovszky, Z., 2006. Partitioning and budget of Li, Be and B in high-pressure metamorphic rocks. Geochim. Cosmochim. Acta 70, 4750–4769. https://doi.org/10.1016/j.gca.2006.07.006.
Marschall, H.R., Wanless, V.D., Shimizu, N., Pogge von Strandmann, P.A.E., Elliott, T., Monteleone, B.D., 2017. The boron and lithium isotopic composition of mid-ocean ridge basalts and the mantle. Geochim. Cosmochim. Acta 207, 102–138. https://doi.org/10.1016/j.gca.2017.03.028.
Martin, C., Flores, K.E., Harlow, G.E., 2016. Boron isotopic discrimination for subduction-related serpentinites. Geology 44, 899–902. https://doi.org/10.1130/G38102.1.
McArthur, J.M., Howarth, R.J., Shields, G.A., Zhou, Y., 2020. Strontium isotope stratigraphy. In: Geologic Time Scale 2020. Elsevier, pp. 211–238. https://doi.org/10.1016/B978-0-12-824360-2.00007-3.
McDonough, W.F., Sun, S.-s, 1995. The composition of the Earth. Chem. Geol. 120, 223–253.
Moran, A.E., Sisson, V.B., Leeman, W.P., 1992. Boron depletion during progressive metamorphism: Implications for subduction processes. Earth Planet. Sci. 111 (2–4), 331–349.
Morimoto, N., Fabires, J., Ferguson, A.K., Ginzburg, I.V., Ross, M., Aoki, K., Gottardi, G., 1988. Nomenclature of pyroxenes. Am. Mineral. 73, 1123–1133.
Mulder, J., Hagen-Peter, G., Ubide, T., Andreasen, R., Kooijman, E., Kielman-Schmitt, M., Feng, Y.X., Paul, B., Karlsson, A., Tegner, C., Lesher, C., Costa, F., 2023. New reference materials, analytical procedures and data reduction strategies for Sr isotope measurements in geological materials by LA-MC-ICP-MS. Geostand. Geoanal. Res. 47, 311–336. https://doi.org/10.1111/ggr.12480.
Panseri, M., Fontana, E., Tartarotti, P., 2008. Evolution of rodingitic dikes: metasomatism and metamorphism in the Mount Avic serpentinites (Alpine ophiolites, Southern Aosta Valley). Ofioliti 33, 165–185.
Pawley, A., 2003. Chlorite stability in mantle peridotite: the reaction clinochlore + enstatite = forsterite + pyrope + H2O. Contrib. Mineral. Petrol. 144, 449–456. https://doi.org/10.1007/s00410-002-0409-y.
Petriglieri, J.R., Salvioli-Mariani, E., Mantovani, L., Tribaudino, M., Lottici, P.P., Laporte-Magoni, C., Bersani, D., 2015. Micro-Raman mapping of the polymorphs of serpentine. J. Raman Spectrosc. 46, 953–958. https://doi.org/10.1002/jrs.4695.
Piccoli, F., Rubatto, D., Millonig, L.J., Gerdes, A., 2024. Timing of multiple fluid pulses recorded by garnet and accessory minerals in metarodingites. Lithos 482–483. https://doi.org/10.1016/j.lithos.2024.107702.
Prigent, C., Guillot, S., Agard, P., Lemarchand, D., Soret, M., Ulrich, M., 2018. Transfer of subduction fluids into the deforming mantle wedge during nascent subduction: evidence from trace elements and boron isotopes (Semail ophiolite, Oman). Earth Planet. Sci. Lett. 484, 213–228. https://doi.org/10.1016/j.epsl.2017.12.008.
Rehkamper, M., Hofmann, A.W., 1997. Recycled ocean crust and sediment in Indian Ocean MORB. Earth Planet. Sci. Lett. 147, 93–106. https://doi.org/10.1016/S0012-821X(97)00009-5.
Rice, J.M., 1983. Metamorphism of rodingites: part I. Phase relations in a portion of the system CaO-MgO-Al2O3-SiO2-CO2-H2O. Am. J. Sci. 283, 121–150.
Rubatto, D., Scambelluri, M., 2003. U-Pb dating of magmatic zircon and metamorphic baddeleyite in the Ligurian eclogites (Voltri Massif, Western Alps). Contrib. Mineral. Petrol. 146, 341–355. https://doi.org/10.1007/s00410-003-0502-x.
Scambelluri, M., Rampone, E., 1999. Mg-metasomatism of oceanic gabbros and its control on Ti-clinohumite formation during eclogitization. Contrib. Mineral. 135 (1), 1–17.
Scambelluri, M., Müntener, O., Hermann, J., Piccardo, G.B., Trommsdorff, V., 1995. Subduction of water into the mantle: history of an Alpine peridotite. Geology 23, 459–462.
Schwarzenbach, E.M., Vogel, M., Früh-Green, G.L., Boschi, C., 2021. Serpentinization, carbonation, and metasomatism of ultramafic sequences in the northern Apennine Ophiolite (NW Italy). J. Geophys. Res. Solid Earth 126. https://doi.org/10.1029/2020JB020619.
Shen, T.t., Wu, F.y., Zhang, L.f., Hermann, J., Li, X.p., Du, J.x., 2016. In-situ U-Pb dating and Nd isotopic analysis of perovskite from a rodingite blackwall associated with UHP serpentinite from southwestern Tianshan, China. Chem. Geol. 431, 67–82. https://doi.org/10.1016/j.chemgeo.2016.03.029.
Spandler, C., Pirard, C., 2013. Element recycling from subducting slabs to arc crust: a review. Lithos. https://doi.org/10.1016/j.lithos.2013.02.016.
Spandler, C., Hermann, J., Arculus, R., Mavrogenes, J., 2003. Redistribution of trace elements during prograde metamorphism from lawsonite blueschist to eclogite facies; implications for deep subduction-zone processes. Contrib. Mineral. Petrol. 146, 205–222. https://doi.org/10.1007/s00410-003-0495-5.
Spandler, C., Hermann, J., Faure, K., Mavrogenes, J.A., Arculus, R.J., 2008. The importance of talc and chlorite "hybrid" rocks for volatile recycling through subduction zones; evidence from the high-pressure subduction mélange of New Caledonia. Contrib. Mineral. Petrol. 155, 181–198. https://doi.org/10.1007/s00410-007-0236-2.
Spivack, A.J., Edmond, J.M., 1987. Boron isotope exchange between seawater and the oceanic crust. Geochim. Cosmochim. Acta 51, 1033–1043.
Starr, P.G., Broadwell, K.S., Dragovic, B., Scambelluri, M., Haws, A.A., Caddick, M.J., Smye, A.J., Baxter, E.F., 2020. The subduction and exhumation history of the Voltri Ophiolite, Italy: evaluating exhumation mechanisms for high-pressure metamorphic massifs. Lithos 376–377. https://doi.org/10.1016/j.lithos.2020.105767.
Tribuzio, R., Renna, M.R., Dallai, L., Zanetti, A., 2014. The magmatic-hydrothermal transition in the lower oceanic crust: clues from the Ligurian ophiolites, Italy. Geochim. Cosmochim. Acta 130, 188–211. https://doi.org/10.1016/j.gca.2014.01.010.
Ulmer, P., Trommsdorff, V., 1995. Serpentine stability to mantle depths and subduction-related magmatism. Science 1979 (268), 858–860.
Wilson, S.A., 2018. G-Probe 20 Summary Report: International Association of Geoanalysts G-Probe 20 Report, p. 13.
Wu, S., Wörner, G., Jochum, K.P., Stoll, B., Simon, K., Kronz, A., 2019. The preparation and preliminary characterisation of three synthetic andesite reference glass materials (ARM-1, ARM-2, ARM-3) for in situ microanalysis. Geostand. Geoanal. Res. 43, 567–584. https://doi.org/10.1111/ggr.12301.
Xiong, J.W., Chen, Y.X., Scambelluri, M., Qiao, X.Y., Chen, Y., Huang, F., Belmonte, D., Zhao, Z.F., 2024. Fluid-metasomatized rocks with extremely low δ26Mg values in subducted oceanic lithosphere: implications for mantle Mg isotope heterogeneity and the origin of low-δ26Mg magmas. Geochim. Cosmochim. Acta 371, 111–125. https://doi.org/10.1016/j.gca.2024.03.006.
Xu, J., Zhang, G.B., Marschall, H.R., Walters, J.B., Liu, S.Q., Lü, Z., Zhang, L.F., Hu, H., Li, N., 2022. Boron isotopes of white mica and tourmaline in an ultra-high pressure metapelite from the western Tianshan, China: dehydration and metasomatism during exhumation of subducted ocean-floor sediments. Contrib. Mineral. Petrol. 177. https://doi.org/10.1007/s00410-022-01916-7.
Zanoni, D., Rebay, G., Spalla, M.I., 2016. Ocean floor and subduction record in the Zermatt-Saas rodingites, Valtournanche, Western Alps. J. Metam. Geol. 34, 941–961. https://doi.org/10.1111/jmg.12215.
Zhao, H., Zhao, X.M., Le Roux, P.J., Zhang, W., Wang, H., Xie, L.W., Huang, C., Wu, S.T., Yang, J.H., Wu, F.Y., Yang, Y.H., 2020. Natural clinopyroxene reference materials for in situ Sr isotopic analysis via LA-MC-ICP-MS. Front. Chem. 8. https://doi.org/10.3389/fchem.2020.594316.
Zhao, M.S., Chen, Y.X., Xiong, J.W., Qiao, X.Y., Zheng, Y.F., Duan, W.Y., Huang, F., Zhao, Z.F., 2023. Magnesium–oxygen isotope constraints on the origin of rodingites in oceanic lithosphere. Chem. Geol. 635. https://doi.org/10.1016/j.chemgeo.2023.121612.